optica

Ultrabroadband nonlinear optics in nanophotonic periodically poled lithium niobate waveguides

Marc Jankowski,[1,*] Carsten Langrock,[1] Boris Desiatov,[2] Alireza Marandi,[3] Cheng Wang,[4] Mian Zhang,[5] Christopher R. Phillips,[6] Marko Lončar,[2] and M. M. Fejer[1]

[1]Edward L. Ginzton Laboratory, Stanford University, Stanford, California 94305, USA
[2]John A. Paulson School of Engineering and Applied Sciences, Harvard University, Cambridge, Massachusetts 02138, USA
[3]California Institute of Technology, Pasadena, California 91125, USA
[4]Department of Electrical Engineering, State Key Lab of THz and Millimeter Waves, City University of Hong Kong, Kowloon, Hong Kong, China
[5]HyperLight Corporation 501 Massachusetts Avenue, Cambridge, Massachusetts 02139, USA
[6]Department of Physics, Institute of Quantum Electronics, ETH Zurich, Zurich 8093, Switzerland
*Corresponding author: marcjank@stanford.edu

Received 19 September 2019; revised 11 November 2019; accepted 25 November 2019 (Doc. ID 378172); published 7 January 2020

Quasi-phase-matched interactions in waveguides with quadratic nonlinearities enable highly efficient nonlinear frequency conversion. In this paper, we demonstrate the first generation of devices that combine the dispersion engineering available in nanophotonic waveguides with quasi-phase-matched nonlinear interactions available in periodically poled lithium niobate (PPLN). This combination enables quasi-static interactions of femtosecond pulses, reducing the pulse energy requirements by several orders of magnitude compared to conventional devices, from picojoules to femtojoules. We experimentally demonstrate two effects associated with second harmonic generation (SHG). First, we observe efficient quasi-phase-matched SHG with <100 fJ of pulse energy. Second, in the limit of strong phase-mismatch, we observe spectral broadening of both harmonics with as little as 2 pJ of pulse energy. These results lay a foundation for a new class of nonlinear devices, in which coengineering of dispersion with quasi-phase-matching enables efficient nonlinear optics at the femtojoule level.

https://doi.org/10.1364/OPTICA.7.000040

1. INTRODUCTION

Phase-matched interactions in materials with quadratic ($\chi^{(2)}$) nonlinearities are crucial for realizing efficient second harmonic generation (SHG), sum- and difference-frequency generation, and optical parametric amplification. These dynamical processes are used as building blocks in many modern optical systems, including near- and mid-infrared light generation [1,2], ultrashort pulse compression [3], supercontinuum generation [4], frequency comb stabilization [5], upconversion detection and quantum frequency conversion [6], all-optical signal processing [7], coherent Ising machines [8], and the generation of nonclassical states of light [9]. Weakly guiding diffused waveguides in periodically poled ferroelectrics like lithium niobate [10], lithium tantalite [11], and potassium titanyl phosphate [12] are a commonly used platform for such devices. These waveguides are conventionally formed by a small refractive index modulation ($\Delta n \sim 0.02$) due to indiffused dopants and exhibit low-loss (~0.1 dB/cm) modes with field diameters of ~5 μm and quasi-phase-matched interactions between these modes through periodic poling of the $\chi^{(2)}$ coefficient. To date, these devices have suffered largely from two limitations. The power requirements of such devices are set by the largest achievable normalized efficiencies (90%/W-cm^2 for SHG of 1560-nm light [7]), and the phase-matching bandwidths (and hence useful lengths for pulsed interactions) have ultimately been limited by the material dispersion that dominates over geometrical dispersion in weakly guiding waveguides.

Recent efforts have focused on the development of $\chi^{(2)}$ nanophotonics in platforms such as lithium niobate [13], aluminum nitride [14], and gallium arsenide [15]. These systems allow for densely integrated nonlinear photonic devices and achieve efficient frequency conversion due to the large field intensities associated with subwavelength mode confinement. The current state of the art of $\chi^{(2)}$ nanophotonic devices comprises two approaches: modal phase-matching, using the geometric dependence of the phase velocity of TE and TM modes [15–17], and quasi-phase-matching, using waveguides with periodically poled $\chi^{(2)}$ nonlinearities [1,18]. While modal phase-matching has achieved the largest normalized efficiencies to date (13, 000%/W-cm^2 [15]), the waveguide geometry is determined by the conditions in which the phase velocity of the fundamental and second harmonic are matched. These constraints are lifted in quasi-phase-matched waveguides, where the waveguide geometry may be chosen to engineer both the group velocity and the group-velocity dispersion of the interacting waves. The poling period

necessary for quasi-phase-matched interactions is then determined by the phase-velocity mismatch in the chosen waveguide geometry. While engineering of these dispersion orders is often done in centrosymmetric waveguides, where the relative sign of the group velocity dispersion and $\chi^{(3)}$ nonlinearity can be chosen to achieve soliton formation and spectral broadening [5], to date there has been no demonstration of dispersion-engineered quasi-phase-matched $\chi^{(2)}$ interactions.

In this work we use direct-etched nanophotonic PPLN ridge waveguides to provide the first experimental demonstration of ultrabroadband quasi-phase-matched $\chi^{(2)}$ interactions in a dispersion-engineered waveguide. This paper will proceed in three parts: i) we briefly summarize the design and fabrication of nanophotonic PPLN waveguides; ii) we experimentally demonstrate SHG in a dispersion-engineered PPLN waveguide; and iii) we experimentally demonstrate multioctave supercontinuum generation in a phase-mismatched PPLN waveguide. The devices shown in Section 2, which have been designed for broadband SHG of wavelengths around 2-μm, exhibit SHG transfer functions with 3-dB bandwidths of >110 nm and achieve a saturated SHG conversion efficiency in excess of 50% with pulse energies as low as 60 fJ when pumped with 50-fs-long pulses centered around 2 μm. The bandwidth and energy requirements of these waveguides represent an improvement over conventional waveguides by 10× and 30×, respectively. In Section 3, we choose the poling period of these waveguides for phase-mismatched SHG, which leads to self-phase modulation with an effective nonlinearity more than 2 orders of magnitude larger than the pure electronic $\chi^{(3)}$ of lithium niobate. When such a waveguide is driven with pulse energies in excess of 1 pJ it exhibits a cascade of mixing processes, resulting in the generation and spectral broadening of the first five harmonics. The techniques demonstrated here can be generalized to engineer the transfer functions and interaction lengths of any three-wave interaction based on $\chi^{(2)}$ nonlinearities and will allow for many of the dynamical processes used in conventional PPLN devices to be scaled to substantially lower pulse energies.

2. NANOPHOTONIC PPLN WAVEGUIDES

We begin by describing the design and fabrication of nanophotonic PPLN waveguides. A cross-section of a typical ridge waveguide is shown in Fig. 1(a), with the simulated TE_{00} modal field amplitude of the fundamental and second harmonic, respectively. We consider a 700-nm x-cut thin film and examine the roles of etch depth and waveguide width on the performance of the waveguide. For continuous-wave (CW) interactions, the relevant parameters are the poling period needed to achieve phase-matching, and the effective strength of the interaction. The required poling period for SHG is given by $\Lambda = \lambda/(2n_{2\omega} - 2n_{\omega})$, where λ is the wavelength of the fundamental, and $n_{\omega,2\omega}$ is the effective index of the fundamental and second harmonic modes, respectively. The poling period is shown as a function of waveguide geometry in Fig. 1(b) and exhibits a linear scaling in width and etch depth, with larger waveguides having larger poling periods. The typical measure of nonlinearity is the normalized efficiency, η_0, which specifies the efficiency for phase-matched, undepleted, CW SHG in a nonlinear waveguide as $P_{2\omega}/P_{\omega} = \eta_0 P_{\omega} L^2$. η_0 is shown in Fig. 1(c) and scales with the inverse of the area of the waveguide modes,

$$\eta_0 = \frac{2\omega^2 d_{\text{eff}}^2}{n_{\omega}^2 n_{2\omega} \epsilon_0 c^3 A_{\text{eff}}}, \tag{1}$$

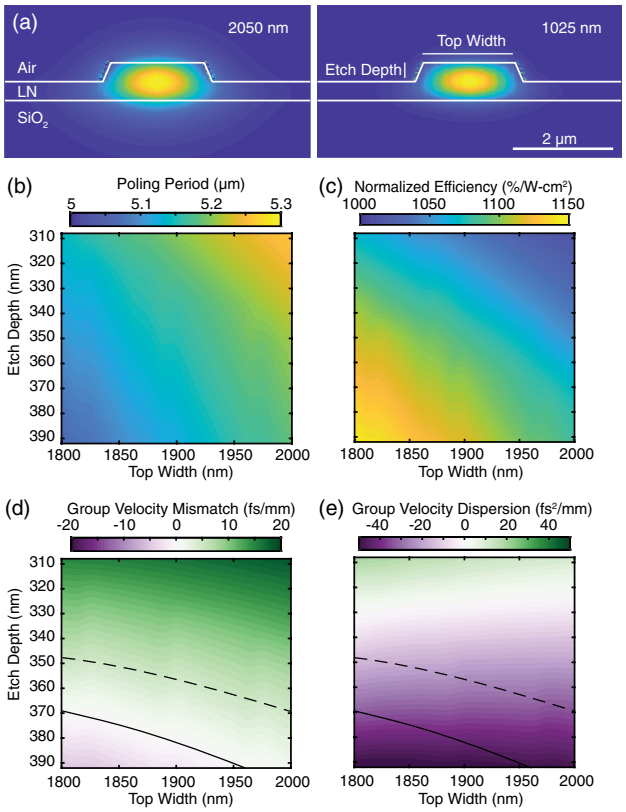

Fig. 1. (a) Waveguide cross-section, showing the normalized electric field associated with the simulated TE_{00} fundamental (left) and second harmonic (right) modes. The waveguides shown here correspond to a top width of 1850 nm, an etch depth of 340 nm, and a starting film thickness of 700 nm. (b) and (c) Simulated poling period and normalized efficiency, respectively, as a function of waveguide geometry. (d) and (e) Simulated $\Delta k'$ and k''_{ω}, respectively. The solid black lines denote $\Delta k' = 0$, and the dashed black contour line shows geometries that achieve $|\Delta k'| < 5$ fs/mm.

where $d_{\text{eff}} = \frac{2}{\pi} d_{33}$ is the effective nonlinear coefficient for quasi-phase-matched interactions that have been poled with a 50% duty cycle and $d_{33} = 20.5$ pm/V for SHG of 2050-nm light. This value is found using a least squares fit to the values reported in [19,20] extrapolated to 2 μm with constant Miller's delta scaling. A_{eff} is the effective area of the interaction and is 1.6 μm^2 for SHG between the modes shown in Fig. 1(a). For a detailed description of the modal overlap integral involved in computing the effective area, we refer the reader to the supplemental.

The role of dispersion will be discussed in more detail in the following sections. We note, for completeness that the bandwidth of nonlinear interactions is usually dominated by mismatch of the inverse group velocities of the interacting waves, hereafter referred to as the temporal walkoff or a group velocity mismatch, $\Delta k'$. In the absence of the temporal walkoff, the group velocity dispersion of the fundamental, k''_{ω}, plays a dominant role. $\Delta k'$ and k''_{ω} are shown in Fig. 1(d) and Fig. 1(e), respectively. Temporal walkoff becomes negligible for etch depths >350-nm, and anomalous dispersion occurs at wavelengths around 2050 nm for etch depths >330-nm.

We conclude this section by briefly summarizing the fabrication of the nanophotonic PPLN waveguides used for the remainder of this paper. First, periodic poling is done as described in [1]. Here, metal electrodes are deposited and patterned on an

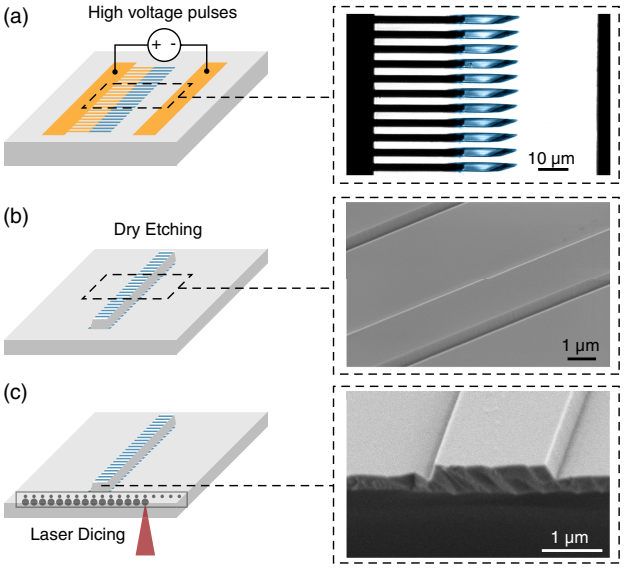

Fig. 2. (a) Schematic of the poling process, resulting in high fidelity domain inversion with a ∼50% duty cycle. (b) Waveguides are patterned using an Ar^+ assisted dry etch, resulting in smooth sidewalls. (c) The samples are prepared using laser dicing, resulting in optical-quality end-facets.

x-cut magnesium-oxide (MgO)-doped lithium niobate thin film (NANOLN). Then, several high voltage pulses are applied to the electrodes, resulting in periodic domain inversions [Fig. 2(a)]. The inset shows a colorized two-photon microscope image of the resulting inverted domains with a duty cycle of ∼50%. Second, waveguides are patterned using electron-beam lithography and dry etched using Ar^+ ions, as described in Ref. [13]. This process yields low-loss (< 0.1-dB/cm) ridge waveguides [Fig. 2(b)]. The inset shows a scanning electron microscope (SEM) image of the ridge waveguides, showing smooth sidewalls. Finally, facet preparation is done using a DISCO DFL7340 laser saw [Fig. 2(c)]. Here, ∼10-μJ pulses are focused into the substrate to create a periodic array of damage spots, which act as nucleation sites for crack propagation. The sample is then cleaved. The inset shows an SEM image of the resulting end-facets, which exhibit ∼10-nm facet roughness.

Using these methods, we fabricated 45 6-mm-long waveguides corresponding to three different top widths and 15 poling periods ranging from 5.01-μm to 5.15-μm. We chose the 10-nm shift between consecutive poling periods to correspond to a shift of ΔkL by 2π and use temperature for fine tuning of the phase-mismatch. The yield for poling and waveguide fabrication was 50% and 90%, respectively, and the coupling efficiency varied from 0.03% to 1% depending on the quality of the end-facet, with 10% of the waveguides exhibiting facet damage. We note here that theoretical coupling efficiencies in excess of 30% are possible with the NA = 0.5 optics used throughout this paper and that further refinements of both the facet preparation recipe and the incoupled Gaussian beam have yielded devices with coupling efficiencies commensurate with theory. For the remainder of this paper we will report pulse energies internal to the waveguide and focus on waveguides with a top width of ∼1850 nm and an etch depth of ∼340 nm, which achieve phase-matching near a period of 5.11-μm. The resulting theoretical normalized efficiency is 1100%/W-cm^2, $\Delta k' = 5$-fs/mm, and $k''_\omega = -15$-fs^2/mm. The calculated value of $\Delta k'$ is 20 times smaller than that of bulk lithium niobate for 2-μm doubling, which allows for substantially longer interaction lengths for femtosecond pulses.

3. SECOND HARMONIC GENERATION

In this section we discuss SHG of femtosecond pulses in a nanophotonic PPLN waveguide. We begin by explaining the role of dispersion engineering in phase-matched interactions, and how ultrabroadband phase-matched interactions become possible with a suitable choice of waveguide geometry. Then, we describe an experimental demonstration of SHG in a dispersion-engineered PPLN waveguide. The performance of these waveguides, as characterized by the SHG transfer function and normalized efficiency, agrees well with theory and represents an improvement over the performance of conventional PPLN devices, in terms of both bandwidth and normalized efficiency, by more than an order of magnitude.

The coupled wave equations for SHG of an ultrafast pulse are

$$\partial_z A_\omega(z,t) = -i\kappa A_{2\omega} A^*_\omega \exp(-i\Delta k z) + \hat{D}_\omega A_\omega, \tag{2a}$$

$$\partial_z A_{2\omega}(z,t) = -i\kappa A^2_\omega \exp(i\Delta k z) - \Delta k' \partial_t A_{2\omega} + \hat{D}_{2\omega} A_{2\omega}, \tag{2b}$$

where A_ω and $A_{2\omega}$ are the complex amplitudes of the modal fields, normalized so that $|A(z,t)|^2$ is the instantaneous power at position z. κ is the nonlinear coupling, $\kappa = \sqrt{\eta_0}$, and Δk is the phase mismatch between the carrier frequencies, $\Delta k = k_{2\omega} - 2k_\omega - 2\pi/\Lambda$. The dispersion operator, $\hat{D}_\omega = \sum_{j=2}^{\infty}[(-i)^{j+1} k^{(j)}_\omega / j!]\partial_t^j$, contains contributions beyond the first order, where $k^{(j)}_\omega$ represents the jth derivative of propagation constant k at frequency ω.

For SHG in the limit where the fundamental wave is undepleted, these equations may be solved using a transfer function approach [21,22]. Here, the response of the second harmonic to the driving nonlinear polarization is computed by filtering the driving polarization with the transfer function for CW SHG. We implement this approach analytically in two steps. First, we calculate the second harmonic envelope that would be generated in the absence of dispersion, $A^{\mathrm{ND}}_{2\omega}(z,t) = -i\kappa A^2_\omega(0,t)z$. Then, the power spectral density associated with this envelope is filtered in the frequency domain, using the CW transfer function for SHG,

$$|A_{2\omega}(z,\Omega)|^2 = \mathrm{sinc}^2(\Delta k(\Omega) z/2)|A^{\mathrm{ND}}_{2\omega}(z,\Omega)|^2. \tag{3}$$

Here, $A_{2\omega}(z,\Omega) = \mathcal{F}\{A_{2\omega}(z,t)\}(\Omega)$ is the Fourier transform of $A_{2\omega}(z,t)$, and Ω is the frequency detuning around 2ω. The dispersion of a nonlinear waveguide modifies the bandwidth of the SHG transfer function through the frequency dependence of $\Delta k(\Omega) = k(2\omega + 2\Omega) - 2k(\omega + \Omega) - 2\pi/\Lambda$. In conventional quasi-phase-matched devices, the bandwidth of the generated second harmonic is typically dominated by the group-velocity mismatch between the fundamental and second harmonic, $\Delta k(\Omega) \approx 2\Delta k'\Omega$, with a corresponding scaling law for the generated second harmonic bandwidth $\Delta\lambda_{\mathrm{SHG}} \propto 1/|\Delta k'|L$. As discussed previously, the geometric dispersion that arises due to tight confinement in a nanophotonic waveguide may substantially alter $\Delta k'$. Ultrabroadband interactions become possible when the geometric dispersion of a tightly confining waveguide achieves $\Delta k' = 0$. For the waveguides fabricated here, both $\Delta k'$ and k''_ω are small. In this case the corresponding SHG bandwidth becomes

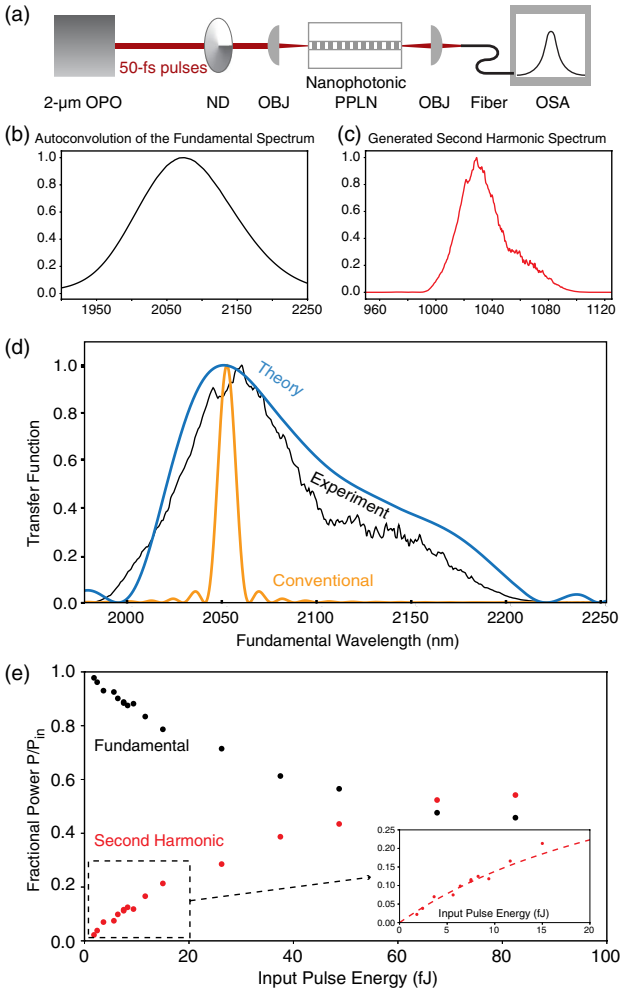

Fig. 3. (a) Schematic of experimental setup. ND, variable neutral density filter; OBJ, reflective objective lens; OSA, optical spectrum analyzer. (b) and (c) Measured spectrum of the driving polarization ($|A_\omega(0,\Omega) * A_\omega(0,\Omega)|^2$) and output second harmonic ($|A_{2\omega}(L,\Omega)|^2$), respectively. (d) Measured SHG transfer function (black) for a 6-mm-long nanophotonic waveguide, showing good agreement with theory (blue). The bandwidth of these waveguides exceeds that of bulk PPLN (orange) by more than an order of magnitude. (e) SHG conversion efficiency and pump depletion as a function of input pulse energy, showing 50% conversion efficiency with an input pulse energy of 60 fJ. Inset: undepleted regime with fit given by Eq. (3) and a heuristic model for saturation, as described in the text.

dominated by higher-order dispersion, and $\Delta k(\Omega)$ must be calculated using the full dispersion relations of the TE_{00} fundamental and second harmonic modes.

The experimental setup is shown in Fig. 3(a). We characterize the behavior of the nanophotonic PPLN waveguides using nearly transform-limited 50-fs-long pulses from a synchronously pumped degenerate optical parametric oscillator (OPO). The OPO used here is identical to that described in Ref. [23], except that the cavity has a repetition frequency of 75 MHz. We use reflective inverse-cassegrain lenses (Thorlabs LMM-40X-P01) both to couple into the sample and to collect the output. This ensures that the incoupled pulses are chirp-free and that the collected harmonics are free of chromatic aberrations. To characterize the SHG transfer function, we record the spectrum input to the waveguide at the fundamental and output from the waveguide at the second harmonic. Then, we estimate $A_{2\omega}^{\mathrm{ND}}(z,\Omega) \propto A_\omega(z,\Omega) * A_\omega(z,\Omega)$ using the autoconvolution of the spectrum of the fundamental, shown in Fig. 3(b). The ratio of the measured second harmonic spectrum [Fig. 3(c)] with $A_{2\omega}^{\mathrm{ND}}$ yields the measured SHG transfer function [Fig. 3(d)], showing good agreement between experiment and theory. These devices exhibit a 3-dB bandwidth > 110 nm, which outperforms bulk 2-μm SHG devices of the same length in PPLN by an order of magnitude. This broad transfer function confirms that the waveguide achieves quasi-static interactions of short pulses across the length of the device. Furthermore, the strong agreement between the measured and theoretical transfer function verifies the calculated waveguide dispersion. The conversion efficiency of the second harmonic and depletion of the fundamental input to the waveguide is shown as a function of input pulse energy in Fig. 3(e). The inset shows the undepleted regime, denoted by the dotted box in Fig. 3(e). The dotted line is a theoretical fit of Eq. (3), where we have accounted for a small degree of saturation at the peak of the pulse by using $A_{2\omega}^{\mathrm{ND}}(z,t) = -iA_\omega(0,t)\tanh(\kappa A_\omega(0,t)z)$. The only fitting parameter used here is a peak CW normalized efficiency of 1000%/W-cm^2, which agrees well with the theoretically predicted value of 1100%/W-cm^2, and represents a 45-fold improvement over conventional 2-μm SHG devices based on proton-exchanged waveguides. When this large CW normalized efficiency is combined with the peak field associated with a 50-fs-long pulse these waveguides achieve 50% conversion efficiency for an input pulse energy of only 60-fJ, which is a 30-fold reduction compared to the state of the art [24].

4. SUPERCONTINUUM GENERATION

In this section we discuss spectral broadening by cascaded nonlinearities in a nanophotonic PPLN waveguide. We begin by introducing a heuristic picture based on cascaded nonlinearities in phase-mismatched SHG and discuss the role of dispersion. Based on this heuristic picture, we show that the effective nonlinearity of these waveguides exceeds that of conventional $\chi^{(3)}$-based devices, including nanophotonic silicon waveguides. We then describe an experimental demonstration of supercontinuum generation (SCG) in a dispersion-engineered PPLN waveguide. The performance of these waveguides, as characterized by the pulse energies required to generate an octave of bandwidth at multiple harmonics, is an improvement over previous demonstrations in lithium niobate by more than an order of magnitude.

In the limit of a large phase-mismatch, self-phase modulation of the fundamental occurs due to back-action of the second harmonic on the fundamental. This can be seen by reducing the coupled wave equations to an effective nonlinear Schrödinger equation for the fundamental wave [3,25]. We neglect dispersion beyond the second order and assume the phase mismatch is sufficiently large to satisfy two criteria: $|\Delta k| \gg \kappa A_0$, where $A_0 = \max(|A_\omega(0,t)|)$, and $|\Delta k| \gg 4\pi|\Delta k'/\tau|$, where τ is the transform-limited duration of the pulse input to the waveguide. Under these conditions, Eqs. (2a) and (2b) become

$$\partial_z A_\omega = \frac{ik''_\omega}{2}\partial_t^2 A_\omega + i\gamma_{\mathrm{SPM}}|A_\omega^2|A_\omega, \tag{4}$$

where $\gamma_{SPM} = -\eta_0/\Delta k$. Typically, the bounds on Δk, and thus the strength of the effective self-phase modulation, are set by the temporal walkoff. This constraint is lifted when $\Delta k' \sim 0$. For modest values of the phase mismatch ($\Delta k \sim 1\ \mathrm{mm}^{-1}$) and the CW normalized efficiency measured previously, the effective nonlinearity is $\gamma_{SPM} = 100/\mathrm{W\text{-}m}$. This corresponds to an effective nonlinear refractive index of $n_2 = 4.8 \times 10^{-17}\ \mathrm{m}^2/\mathrm{W}$. We may compare this to the n_2 associated with Kerr nonlinearities in lithium niobate by scaling the values found in [4] with a two-band model [26]. We find $n_2 = 2.6 \times 10^{-19}\ \mathrm{m}^2/\mathrm{W}$ at 2050 nm, which is nearly 200 times weaker than the self-phase modulation due to cascaded nonlinearities. The γ_{SPM} shown here also exceeds typical values in common nanophotonic platforms using Kerr nonlinearities. Recent demonstrations of SCG in silicon, silicon nitride, and lithium niobate achieved a γ_{SPM} of 38/W-m, 3.25/W-m, and 0.4/W-m, respectively [5,27,28].

In addition to an enhanced nonlinearity, phase-mismatched SHG also generates a spectrally broadened second harmonic. Within the approximations made here the phase mismatch is constant across the bandwidth of the input pulse, $\Delta k(\Omega) \approx \Delta k(0)$, and the second harmonic is given by

$$A_{2\omega}(z, t) = -i\kappa A_{\omega}(z, t)^2 (\exp(i\Delta k z) - 1)/\Delta k. \quad (5)$$

Here, the time varying phase envelope of the fundamental directly produces a rapidly varying phase of the second harmonic, $\phi_{2\omega}(z, t) \sim 2\phi_{\omega}(z, t)$. Thus, we expect both harmonics to exhibit spectral broadening as the fundamental undergoes self-phase modulation. In practice, the full nonlinear polarization generates a cascade of mixing processes that leads to spectral broadening of several harmonics; a heuristic picture of this process is beyond the scope of this paper.

We characterize SCG in a nanophotonic PPLN waveguide with the OPO source and waveguide geometry used in the SHG experiment; however we now choose a 5.10-μm poling period such that $\Delta k L = -3\pi$. We record the output spectrum from the waveguide using three spectrometers: the visible to near-infrared (400–900 nm) range is captured with a Ocean Optics USB4000, the near- to mid-infrared (900–1600 nm) is captured with a Yokogawa AQ6370C, and the mid-infrared (1600–2400 nm) is captured using a Yokogawa AQ6375. The results are shown in Fig. 4. The fundamental, second harmonic, and fourth harmonic are observed for input pulse energies as low as 0.5 pJ. For pulse energies >1 pJ, the first two harmonics undergo spectral broadening, and we observe buildup of the third harmonic. As the waveguide is driven with larger pulse energies, all of the observed harmonics undergo spectral broadening. The first two harmonics merge into a supercontinuum spanning more than an octave when driven with 2-pJ of pulse energy. When driven with pulse energies in excess of 10 pJ, the first five harmonics undergo spectral broadening and merge together to form a supercontinuum spanning >2.5 octaves at the −30-dB level. The measured supercontinuum is limited to wavelengths >400 nm by the transparency window of our collection optics and <2400 nm by our available spectrometers. A photograph of the multi-octave supercontinuum is shown in Fig. 4(b). The observed diffraction pattern is due to lateral leakage of visible frequencies into slab modes [29]. The evanescent tails of these modes sample the periodic substrate damage from laser dicing, which acts as a diffraction grating.

To characterize the coherence of this multioctave supercontinuum, we measure the carrier-envelope-offset frequency (f_{ceo})

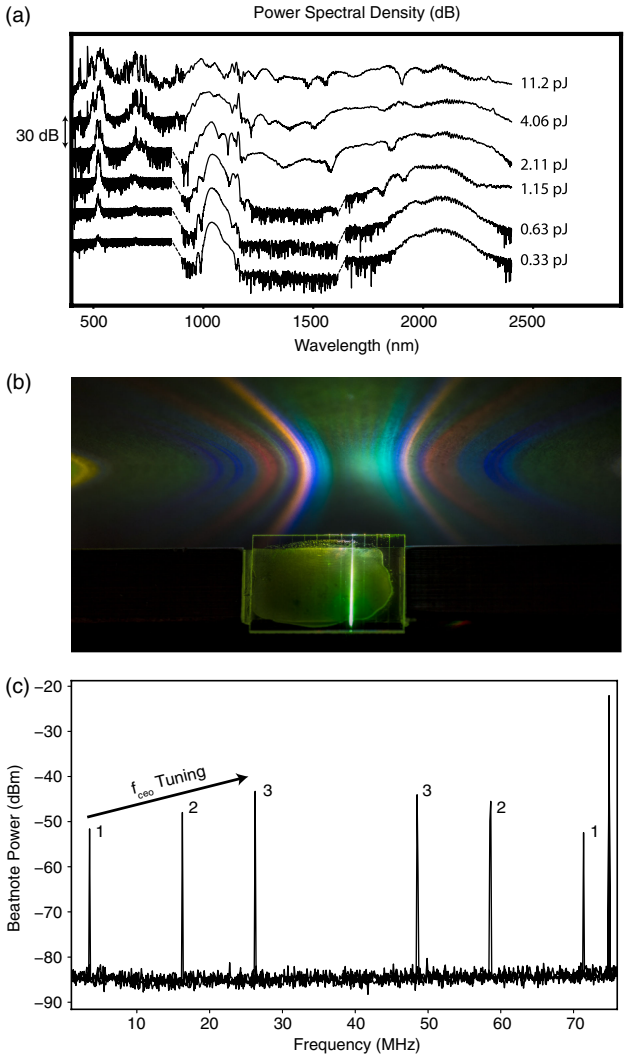

Fig. 4. (a) Evolution of power spectral density over an order of magnitude variation of pulse energy. Adjacent traces are displaced by 30 dB for clarity. The different noise floors correspond to the three spectrometers used, and dotted lines have been added to guide the eye where discontinuities in these noise floors are present. (b) Photograph of supercontinuum produced with 11-pJ input to the waveguide. (c) Measured carrier-envelope-offset beatnotes for three different values of intracavity dispersion in the laser used to pump the OPO.

using beatnotes that arise due to the overlap of the fundamental and second harmonic. The experimental setup is the same as for SHG and SCG, except that the light output from the waveguide is filtered using a Thorlabs FELH-1350 longpass filter and focused onto a Hamamatsu C12668-02 InGaAs photoreceiver. The recorded f_{ceo} beatnotes are shown in Fig. 4(c), alongside a 75-MHz beatnote corresponding to the repetition frequency of the OPO. We verify that the observed beatnotes correspond to the f_{ceo} by tuning the f_{ceo} of the OPO in two steps: (i) we tune the f_{ceo} of the laser used to pump the OPO by translating an intracavity prism, and (ii) we monitor the spectrum of the OPO to verify that it maintains degenerate operation, and therefore remains phase-locked to the pump laser as the f_{ceo} is tuned. We achieve a 35-dB signal-to-noise ratio in a 3-kHz resolution bandwidth, limited by the noise floor of the photoreceiver. Furthermore, we remark that the intensity of the f_{ceo} beatnotes is only ∼22-dB below the intensity

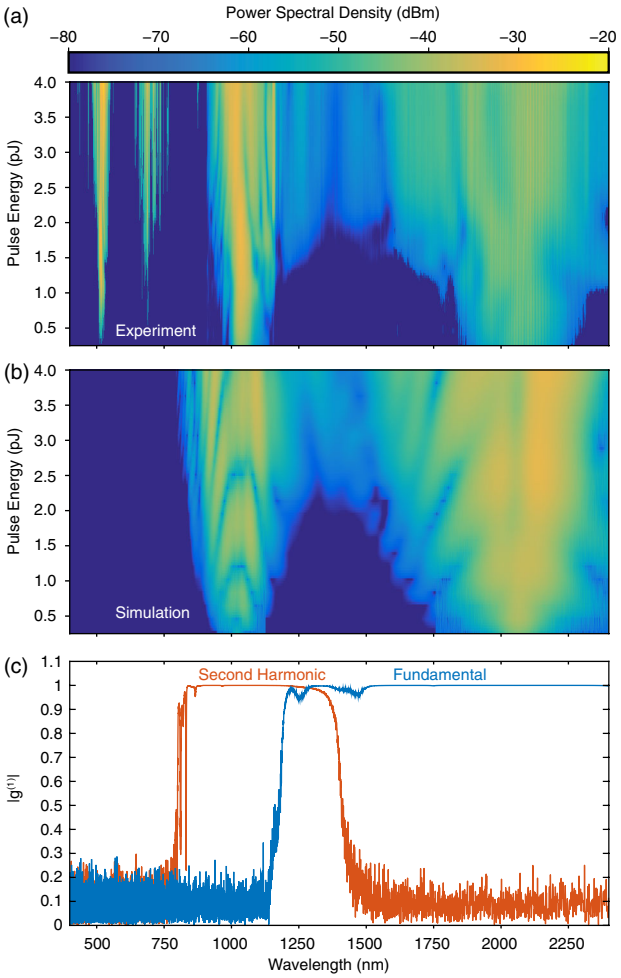

Fig. 5. Power spectral density output from the chip as a function of input pulse energy. (a) Experiment, (b) simulation. The power in dBm is measured in 2-nm-wide spectral bins. (c) Simulated coherence of the fundamental and second harmonic generated by a 4-pJ pulse, showing $|g^{(1)}| \sim 1$.

of the repetition frequency beatnote. This bright relative intensity is due to the beatnotes remaining coherent and inphase across the entire 400-nm-wide bandwidth incident on the photodetector.

To better understand the dynamics and coherence properties of the generated supercontinuum, we simulate Eqs. (2a) and (2b) numerically using the split-step Fourier method described in Ref. [30], which accounts for dispersion to the third order and saturation. The experimentally measured and simulated spectra output from the waveguide are shown in Figures 5(a) and 5(b), respectively. We note that the simulation includes semiclassical vacuum noise and that the results have been renormalized to account for outcoupling such that the simulation and experiment have the same peak power spectral density in the near-infrared band (900–1600 nm) when driven with a pulse energy of 4 pJ. The two-envelope model used here captures many of the features of the experiment except for the buildup of the higher harmonics, which have been explicitly neglected by considering only A_ω and $A_{2\omega}$ in the coupled wave equations. The observed spectral broadening agrees well with traditional heuristics derived from the nonlinear Schrödinger equation, which confirms that this broadening is due to a strong effective γ_{SPM} that arises from back-action of the second harmonic on the fundamental. If we define the soliton number as $N^2 = \gamma_{\mathrm{SPM}} U \tau_s / (2k''_\omega)$, where U is the input pulse energy, and $\tau_s = \tau/1.76$, then the soliton fission length is given by $L_s = \tau_s^2 / N k''_\omega$. The soliton fission length approaches the length of the device for an input pulse energy of 1 pJ, which is the energy at which the observed output spectra begin to exhibit spectral broadening. Supercontinuum generation occurs for pulse energies in excess of 2 pJ. Figure 5(c) shows the simulated coherence function, $|g^{(1)}(\lambda, 0)|$ [31], which has been calculated using an ensemble average of 100 simulations, for an input pulse energy of 4 pJ (N = 14). The simulations shown here suggest that the spectra are coherent over the range of pulse energies considered, with a calculated $\langle |g^{(1)}| \rangle = \int |g^{(1)}(\lambda, 0)| |A(\lambda)|^2 \mathrm{d}\lambda / \int |A(\lambda)|^2 \mathrm{d}\lambda$ of 0.9996 and 0.9990 for the fundamental and second harmonic, respectively. This suggests that decoherence mechanisms that arise due to back-action, such as modulation instabilities, are absent for the devices under study. However, we note that the approach used here neglects many possible decoherence mechanisms, such as degenerate parametric fluorescence of the third harmonic. Further theoretical and experimental study of the coherence properties of these supercontinua will be the subject of future work.

5. CONCLUSION

We have experimentally demonstrated both SHG and SCG in a dispersion-engineered nanophotonic PPLN waveguide. These waveguides are shown to exceed the performance of current-generation SHG devices by at least an order of magnitude in phase-matching bandwidth and pulse energy requirements. Similarly, they achieve self-phase modulation with larger nonlinearities than nanophotonic waveguides based on $\chi^{(3)}$ nonlinearities. These waveguides produce coherent multioctave supercontinua comprising multiple spectrally broadened harmonics with at least an order of magnitude less pulse energy than previous demonstrations in lithium niobate waveguides. These dramatic reductions in energy requirements are made possible by combining the dispersion engineering and large η_0 available in nanophotonic waveguides with periodically poled $\chi^{(2)}$ nonlinearities. When these techniques are combined, they achieve highly efficient quasi-phase-matched interactions of femtosecond pulses over long propagation lengths, thereby enabling a new class of nonlinear photonic devices and systems.

Funding. National Science Foundation (ECCS-1609549, ECCS-1609688, EFMA-1741651); Air Force Office of Scientific Research (MURI FA9550-14-1-0389); Army Research Laboratory (W911NF-15-2-0060, W911NF-18-1-0285).

Acknowledgment. Patterning and dry etching was performed at the Harvard University Center for Nanoscale Systems (CNS), a member of the National Nanotechnology Coordinated Infrastructure (NNCI) supported by the National Science Foundation (NSF). Electrode definition and periodic poling was performed at the Stanford Nano Shared Facilities (SNSF), supported by the NSF. The authors thank Jingshi Chi at DISCO HI-TEC America for her expertise with laser dicing lithium niobate.

Disclosures. The authors declare no conflicts of interest.

See Supplement 1 for supporting content.

REFERENCES

1. C. Wang, C. Langrock, A. Marandi, M. Jankowski, M. Zhang, B. Desiatov, M. M. Fejer, and M. Lončar, "Ultrahigh-efficiency wavelength conversion in nanophotonic periodically poled lithium niobate waveguides," Optica **5**, 1438–1441 (2018).
2. A. S. Mayer, C. R. Phillips, C. Langrock, A. Klenner, A. R. Johnson, K. Luke, Y. Okawachi, M. Lipson, A. L. Gaeta, M. M. Fejer, and U. Keller, "Offset-free gigahertz midinfrared frequency comb based on optical parametric amplification in a periodically poled lithium niobate waveguide," Phys. Rev. Appl. **6**, 054009 (2016).
3. M. Bache, J. Moses, and F. W. Wise, "Scaling laws for soliton pulse compression by cascaded quadratic nonlinearities," J. Opt. Soc. Am. B **24**, 2752–2762 (2007).
4. C. R. Phillips, C. Langrock, J. S. Pelc, M. M. Fejer, I. Hartl, and M. E. Fermann, "Supercontinuum generation in quasi-phasematched waveguides," Opt. Express **19**, 18754–18773 (2011).
5. A. S. Mayer, A. Klenner, A. R. Johnson, K. Luke, M. R. E. Lamont, Y. Okawachi, M. Lipson, A. L. Gaeta, and U. Keller, "Frequency comb offset detection using supercontinuum generation in silicon nitride waveguides," Opt. Express **23**, 15440–15451 (2015).
6. J. S. Pelc, L. Ma, C. R. Phillips, Q. Zhang, C. Langrock, O. Slattery, X. Tang, and M. M. Fejer, "Long-wavelength-pumped upconversion single-photon detector at 1550 nm: performance and noise analysis," Opt. Express **19**, 21445–21456 (2011).
7. C. Langrock, S. Kumar, J. E. McGeehan, A. E. Willner, and M. M. Fejer, "All-optical signal processing using $\chi^{(2)}$ nonlinearities in guided-wave devices," J. Lightwave Technol. **24**, 2579–2592 (2006).
8. P. L. McMahon, A. Marandi, Y. Haribara, R. Hamerly, C. Langrock, S. Tamat, T. Inagaki, H. Takesue, S. Utsunomiya, K. Aihara, R. L. Byer, M. M. Fejer, H. Mabuchi, and Y. Yamamoto, "A fully programmable 100-spin coherent Ising machine with all-to-all connections," Science **354**, 614–617 (2016).
9. H. S. Zhong, Y. Li, W. Li, L. C. Peng, Z. E. Su, Y. Hu, Y. M. He, X. Ding, W. Zhang, H. Li, L. Zhang, Z. Wang, L. You, X. L. Wang, X. Jiang, L. Li, Y. A. Chen, N. L. Liu, C. Y. Lu, and J. W. Pan, "12-photon entanglement and scalable scattershot Boson sampling with optimal entangled-photon pairs from parametric down-conversion," Phys. Rev. Lett. **121**, 250505 (2018).
10. M. Stefszky, V. Ulvila, Z. Abdallah, C. Silberhorn, and M. Vainio, "Towards optical-frequency-comb generation in continuous-wave-pumped titanium-indiffused lithium-niobate waveguide resonators," Phys. Rev. A **98**, 053850 (2018).
11. S. Matsumoto, E. J. Lim, H. M. Hertz, and M. M. Fejer, "Quasiphase-matched second harmonic generation of blue light in electrically periodically-poled lithium tantalate waveguides," Electron. Lett. **27**, 22–23 (1991).
12. M. Fiorentino, S. M. Spillane, R. G. Beausoleil, T. D. Roberts, P. Battle, and M. W. Munro, "Spontaneous parametric down-conversion in periodically poled KTP waveguides and bulk crystals," Opt. Express **15**, 7479–7488 (2007).
13. M. Zhang, C. Wang, R. Cheng, A. Shams-Ansari, and M. Lončar, "Monolithic ultra-high-Q lithium niobate microring resonator," Optica **4**, 1536–1537 (2017).
14. X. Liu, A. W. Bruch, Z. Gong, J. Lu, J. B. Surya, L. Zhang, J. Wang, J. Yan, and H. X. Tang, "Ultra-high-Q UV microring resonators based on a single-crystalline AlN platform," Optica **5**, 1279–1282 (2018).
15. L. Chang, A. Boes, X. Guo, D. T. Spencer, M. J. Kennedy, J. D. Peters, N. Volet, J. Chiles, A. Kowligy, N. Nader, D. D. Hickstein, E. J. Stanton, S. A. Diddams, S. B. Papp, and J. E. Bowers, "Heterogeneously integrated GaAs waveguides on insulator for efficient frequency conversion," Laser Photon. Rev. **12**, 1800149 (2018).
16. A. W. Bruch, X. Liu, X. Guo, J. B. Surya, Z. Gong, L. Zhang, J. Wang, J. Yan, and H. X. Tang, "17000%/W second-harmonic conversion efficiency in single-crystalline aluminum nitride ring resonators," Appl. Phys. Lett. **113**, 131102 (2018).
17. R. Luo, Y. He, H. Liang, M. Li, J. Ling, and Q. Lin, "Optical parametric generation in a lithium niobate microring with modal phase matching," Phys. Rev. Appl. **11**, 034026 (2019).
18. L. Chang, Y. Li, N. Volet, L. Wang, J. Peters, and J. E. Bowers, "Thin film wavelength converters for photonic integrated circuits," Optica **3**, 531–535 (2016).
19. I. Shoji, T. Kondo, A. Kitamoto, M. Shirane, and R. Ito, "Absolute scale of second-order nonlinear-optical coefficients," J. Opt. Soc. Am. B **14**, 2268–2294 (1997).
20. M. M. Choy and R. L. Byer, "Accurate second-order susceptibility measurements of visible and infrared nonlinear crystals," Phys. Rev. B **14**, 1693–1706 (1976).
21. G. Imeshev, M. A. Arbore, S. Kasriel, and M. M. Fejer, "Pulse shaping and compression by second-harmonic generation with quasi-phase-matching gratings in the presence of arbitrary dispersion," J. Opt. Soc. Am. B **17**, 1420–1437 (2000).
22. G. Imeshev, M. A. Arbore, M. M. Fejer, A. Galvanauskas, M. Fermann, and D. Harter, "Ultrashort-pulse second-harmonic generation with longitudinally nonuniform quasi-phase-matching gratings: pulse compression and shaping," J. Opt. Soc. Am. B **17**, 304–318 (2000).
23. A. Marandi, K. A. Ingold, M. Jankowski, and R. L. Byer, "Cascaded half-harmonic generation of femtosecond frequency combs in the mid-infrared," Optica **3**, 324–327 (2016).
24. Z. Zheng, A. M. Weiner, K. R. Parameswaran, M. H. Chou, and M. M. Fejer, "Femtosecond second-harmonic generation in periodically poled lithium niobate waveguides with simultaneous strong pump depletion and group-velocity walk-off," J. Opt. Soc. Am. B **19**, 839–848 (2002).
25. C. Conti, S. Trillo, P. Di Trapani, J. Kilius, A. Bramati, S. Minardi, W. Chinaglia, and G. Valiulis, "Effective lensing effects in parametric frequency conversion," J. Opt. Soc. Am. B **19**, 852–859 (2002).
26. M. Sheik-Bahae, D. J. Hagan, and E. W. Van Stryland, "Dispersion and band-gap scaling of the electronic Kerr effect in solids associated with two-photon absorption," Phys. Rev. Lett. **65**, 96–99 (1990).
27. B. Kuyken, T. Ideguchi, S. Holzner, M. Yan, T. W. Hänsch, J. Van Campenhout, P. Verheyen, S. Coen, F. Leo, R. Baets, G. Roelkens, and N. Picqué, "An octave-spanning mid-infrared frequency comb generated in a silicon nanophotonic wire waveguide," Nat. Commun. **6**, 6310 (2015).
28. J. Lu, J. B. Surya, X. Liu, Y. Xu, and H. X. Tang, "Octave-spanning supercontinuum generation in nanoscale lithium niobate waveguides," Opt. Lett. **44**, 1492–1495 (2019).
29. A. Boes, L. Chang, M. Knoerzer, T. G. Nguyen, J. D. Peters, J. E. Bowers, and A. Mitchell, "Improved second harmonic performance in periodically poled LNOI waveguides through engineering of lateral leakage," Opt. Express **27**, 23919–23928 (2019).
30. M. Jankowski, A. Marandi, C. R. Phillips, R. Hamerly, K. A. Ingold, R. L. Byer, and M. M. Fejer, "Temporal simultons in optical parametric oscillators," Phys. Rev. Lett. **120**, 053904 (2018).
31. J. M. Dudley, G. Genty, and S. Coen, "Supercontinuum generation in photonic crystal fiber," Rev. Mod. Phys. **78**, 1135–1184 (2006).